



Multi-stimuli manipulation of antiferromagnetic domains assessed by second-harmonic imaging

Jean-Yves Chauleau, Eloi Haltz, C. Carretero, S. Fusil, Michel Viret

► To cite this version:

Jean-Yves Chauleau, Eloi Haltz, C. Carretero, S. Fusil, Michel Viret. Multi-stimuli manipulation of antiferromagnetic domains assessed by second-harmonic imaging. *Nature Materials*, 2017, 16, pp.803 - 807. 10.1063/1.3036526 . cea-01591363

HAL Id: cea-01591363

<https://cea.hal.science/cea-01591363>

Submitted on 21 Sep 2017

HAL is a multi-disciplinary open access archive for the deposit and dissemination of scientific research documents, whether they are published or not. The documents may come from teaching and research institutions in France or abroad, or from public or private research centers.

L'archive ouverte pluridisciplinaire **HAL**, est destinée au dépôt et à la diffusion de documents scientifiques de niveau recherche, publiés ou non, émanant des établissements d'enseignement et de recherche français ou étrangers, des laboratoires publics ou privés.

Multi-stimuli manipulation of antiferromagnetic domains assessed by second-harmonic imaging

J.-Y. Chauleau^{1†}, E. Haltz¹, C. Carrétéro², S. Fusil² and M. Viret^{1*}

Among the variety of magnetic textures available in nature, antiferromagnetism is one of the most ‘discrete’ because of the exact cancellation of its staggered internal magnetization. It is therefore very challenging to probe. However, its insensitivity to external magnetic perturbations, together with the intrinsic sub-picosecond dynamics, make it very appealing for tomorrow’s information technologies¹. Thus, it is essential to understand the microscopic mechanisms governing antiferromagnetic domains to achieve accurate manipulation and control. Using optical second-harmonic generation, a unique and laboratory-available tool², we succeeded in imaging with sub-micrometre resolution both electric and antiferromagnetic orders in the model multiferroic BiFeO₃. We show here that antiferromagnetic domains can be manipulated with low power consumption, using sub-coercive electric fields and sub-picosecond light pulses. Interestingly, we also show that antiferromagnetic and ferroelectric domains can behave independently, thus revealing that magneto-electric coupling can lead to various arrangements of the two orders.

Many antiferromagnets possess coupled order parameters which can be used to indirectly influence their magnetic properties. The main one is strain, or structural distortions, such as the slight rhombohedral deformation of the face-centred cubic unit cell of nickel oxide (NiO). This also allows one to indirectly probe the AF domains via the induced birefringence in NiO³. In the well-known ferroelectric (FE) multiferroics, this task could be achieved in an elegant alternative fashion, as the antiferromagnetic (AF) order is often coupled to the ferroelectric polarization. Bismuth ferrite is the archetype of such materials⁴, as it is simultaneously ferroelectric and antiferromagnetic, with both ordering points above room temperature. Our aim here is to demonstrate that electric fields can efficiently change the AF domain configuration in multiferroic BiFeO₃ even without affecting the ferroelectric state. Probing the AF order has always been a hard task, rendered especially difficult by the absence of magnetic stray fields. Most recent publications dealing with spintronic applications of antiferromagnets rely on resistance measurements based on the anisotropic magneto-resistance phenomenon^{5,6}. Although electrical measurements are very useful, imaging magnetic textures is required for a deeper understanding of reversal processes. Among the various available techniques, X-ray-based imaging has recently provided highly resolved images of AF domains in several materials, including NiO^{7,8} and BiFeO₃ (ref. 9), although charging issues do exist for good insulators. On the other hand, nonlinear optics, and in particular second-harmonic generation (SHG), has proven to be a powerful technique to probe complex structural and magnetic distributions^{10,11}. It is well suited to image insulators, with a resolution limited by the wavelength of light involved in

the frequency doubling process, thus in principle allowing sub-micrometre resolution and real-time imaging of AF domains. This is essential to study the response of antiferromagnets to external stimuli, including the important properties of nucleation and propagation of their domain walls.

The material studied here consists of a 110-nm-thick epitaxial film of BiFeO₃ (BFO) grown by pulsed laser deposition on a SrTiO₃ (001) substrate with a 5 nm buffer layer of conducting SrRuO₃ (SRO) (see Methods). The strain imposed by the substrate leads to the disappearance of the cycloidal magnetic order present in the bulk in favour of a slightly canted AF phase¹² arising from the Dzyaloshinskii–Moriya interaction. At room temperature, the BiFeO₃ layer adopts a rhombohedral-like (3 m) crystallographic structure with a small monoclinic distortion. The spontaneous electric polarization (P_s) lies along the [111] directions, thus defining eight possible ferroelectric variants (Fig. 1a). The AF order is G-type, where the spins carried by the Fe³⁺ ions belong to the (111) planes orthogonal to P_s (Fig. 1c–e). Within these planes, a threefold magneto-crystalline anisotropy should lead to three possible directions for the AF vectors, similarly to the archetypal NiO¹³.

The as-grown films are composed of small (100 nm size) ferroelectric domains with polarization predominantly pointing towards the conducting SRO, and different in-plane components distributed along the four possible in-plane orientations (Fig. 1f,g). The tip of a piezoresponse force microscope (PFM) was then used to electrically write polarization domains, and a special effort was devoted to produce single domains (Fig. 1h,i): the out-of-plane component of the polarization was controlled by the above coercive bias applied between the scanning tip and the bottom SrRuO₃ electrode. The in-plane component was simultaneously defined thanks to the ‘trailing field’¹⁴ induced by the tip motion and aligned along the targeted polarization variant. Large single domains (Fig. 1b) are reproducibly obtained, as for instance the 10 $\mu\text{m} \times 10 \mu\text{m}$ square of Fig. 1h,i. We can therefore dispose of different areas where the ferroelectric order is defined at will in which AF properties can be studied by SHG imaging.

In the electron-dipole approximation, the SHG source term $S(2\omega)$ is related to the light-induced nonlinear polarization $P(2\omega)$ in the following way: $S(2\omega) = \mu_0 \partial^2 P / \partial t^2$, where:

$$P = \varepsilon_0 (\chi^{(i)} + \chi^{(c)}) : E(\omega) \otimes E(\omega)$$

with $E(\omega)$ the incident light electric field and $\chi^{(i)}$ and $\chi^{(c)}$ the time-invariant and time-noninvariant SHG tensors, associated with the crystallographic (/ ferroelectric) and magnetic orders, respectively. The measured experimental quantity is the emitted SHG intensity: $I_{\text{SHG}} \propto |P|^2$. Figure 2 presents a sketch of the experiment and a set of images where the SHG light is analysed vertically

¹SPEC, CEA, CNRS, Université Paris-Saclay, CEA Saclay, 91191 Gif-Sur-Yvette, France. ²Unité Mixte de Physique, CNRS, Thales, Univ. Paris-Sud, Université Paris-Saclay, 91767 Palaiseau, France. [†]Present address: Synchrotron Soleil, 91190 Saint Aubin, France. *e-mail: michel.viret@cea.fr

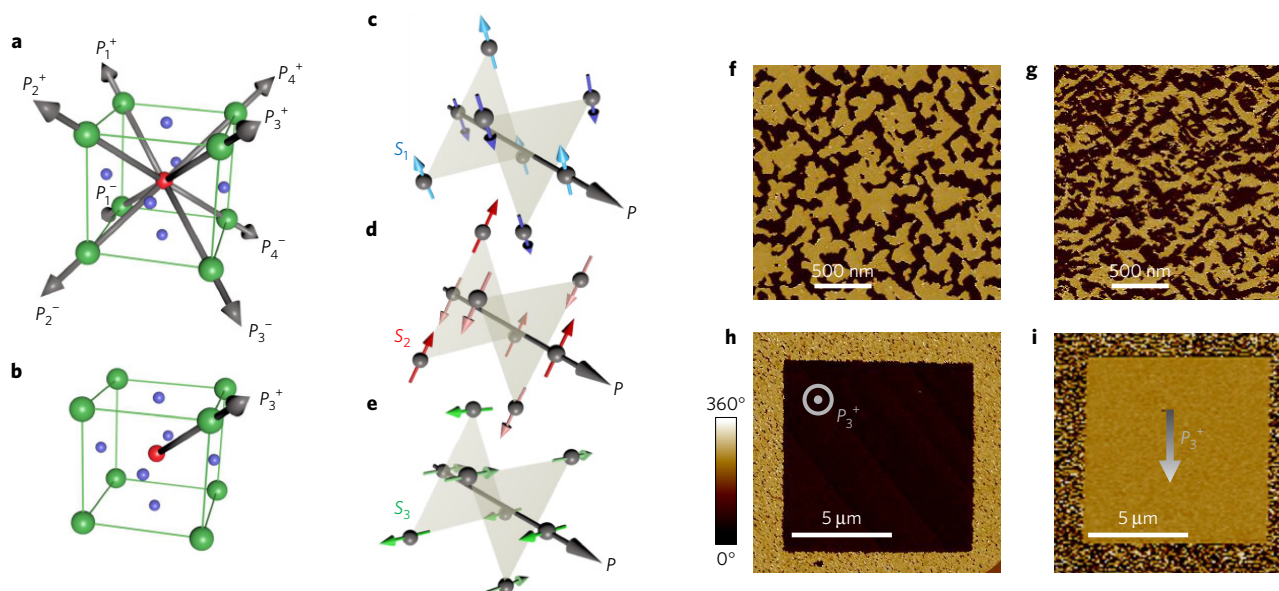


Figure 1 | Ferroelectric configuration of the 001 BiFeO₃ epitaxial layer. **a**, Pseudo-cubic sketch of the eight possible ferroelectric variants, all found in the as-grown film. **b**, Schematics of the spontaneous polarization in the electrically written ferroelectric single domain. **c–e**, Schematic diagrams of the three possible AF domains in a given single FE orientation. **f–g**, 2 × 2 μm out-of-plane and in-plane phase images of the as-grown ferroelectric landscape. **h–i**, Out-of-plane and in-plane phase images of the 10 × 10 μm ferroelectric single domain written by PFM electric poling.

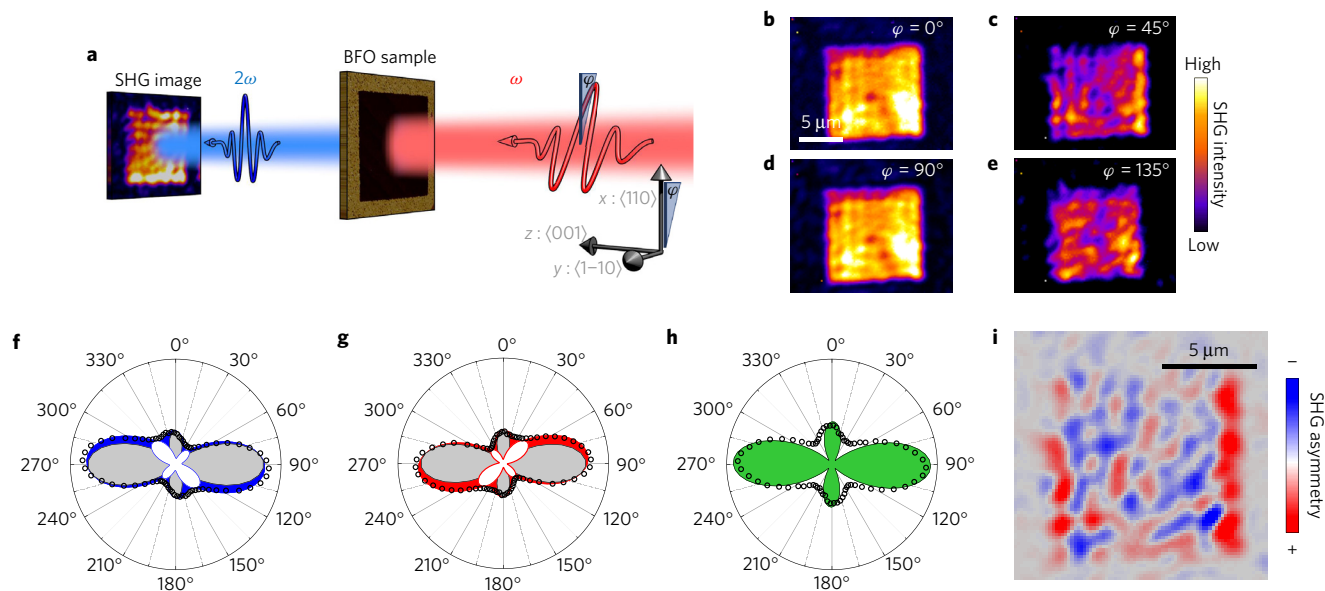


Figure 2 | Second-harmonic generation wide-field imaging. **a**, Diagram of the SHG experiment and the orientation of the (*x*, *y*, *z*) laboratory frame. The light propagates along the *z*-axis corresponding to the [001] crystallographic direction of the BiFeO₃ layer with *x* and *y* along [110] and $\bar{1}\bar{1}0$. **b–e**, Set of typical SHG wide-field images for different linear incident polarizations φ (defined from the *x* axis) and analysed along *x*. The colour scale represents the SHG intensity. **f–h**, Polar plots of the SHG dependence on the incident light polarization direction (with vertical analysis) for the three observed populations. The opened dots are the experimental data. The red, blue and green filled areas are the fits of the SHG data, composed of the time-invariant (ferroelectric) part (grey areas) and the time-noninvariant (antiferromagnetic) part (white areas). **i**, Reconstructed image of the AF texture in our BiFeO₃ sample, where the colour scale represents the asymmetry of the SHG polar plots in **f–h**.

(along the *x*-axis of the laboratory frame) for different directions of polarization of the fundamental light. The incident beam energy is 1.34 eV (wavelength 925 nm), corresponding to a local maximum in the SHG spectral response. Remarkably, substructure patterns can clearly be seen, even in the ferroelectric single-domain region. It is particularly emphasized for specific orientations of the incident light polarization, such as 45° (Fig. 2c) and 135° (Fig. 2e).

We first analyse the SHG by extracting pixel by pixel (about 100 nm × 100 nm) the full angular dependences on incident light polarization. A polar signature composed of two main lobes along the *y* direction and two small lobes along *x*, is systematically observed in the single domain (Fig. 2f–h). This corresponds to the expected contribution from the ferroelectric polarization, described by the time-invariant part of the SHG tensor¹⁵. Interestingly, it turns out that three distinct angular dependences are measured

(Fig. 2f–h). Two of them (f and g) present small asymmetries, which we attribute to the time-noninvariant part of the SHG signal (that is, AF contributions). Their quantitative description can be obtained by rotating the corresponding tensor according to the direction of the AF vector \mathbf{L} (see Methods). The two asymmetric populations, called 1 (Fig. 2f) and 2 (Fig. 2g), correspond to two different AF domains whose in-plane orientations are along the (01) and (10) directions, at 45° to that of \mathbf{P} . The last possible AF domain (number 3) does not produce an asymmetry in the angular dependence on light polarization, as the (11) projection of the AF vector is perpendicular to that of \mathbf{P} . Using this asymmetry criterion and fitting the angular polarization dependence of each pixel, AF domains can be reliably extracted (see Supplementary Methods). Domains of type 1 (blue) and 2 (red) can be unambiguously observed in the written ferroelectric single domain (Fig. 2i). The third domain is harder to single out, as the pixels lacking the asymmetry can also correspond to the borders between domains 1 and 2, where their average produces a symmetrical dependence. Nevertheless, the morphology of the ‘white’ regions looks more like domain walls than extended domains (see Fig. 2i). Moreover, the expected SHG intensity of domain 3 should theoretically fall to ‘zero’ (measurement noise level) for light polarized at 45° and 135° , which is not observed in Fig. 2h. We thus conclude that domain 3 is practically missing. This can be understood, as the small monoclinic distortion imposed in the film by the substrate may lift the degeneracy between the three possible AF domains. Indeed, some anisotropy is added along (001), making domain 3 (the only one with \mathbf{L} perpendicular to (001)) higher in energy. This is further enhanced by the demagnetizing energy induced by the uncompensated magnetic moments resulting from the slight canting of \mathbf{L} (expected to be both perpendicular to \mathbf{P} and \mathbf{L}). Domain 3 being the one with the uncompensated \mathbf{M} closest to the out-of-plane direction, this contributes to increasing its energy. Experimentally, it is also worth mentioning that domain walls jump sideways on micrometre length scales at an observed rate of two or three of these events per month.

Another interesting observation concerns the typical size of AF domains, which is in the micrometre range—that is, a single ferroelectric domain corresponds to a complex AF landscape. The interaction between the two orders is non-trivial as micrometre-sized AF domains are even observed in the as-grown regions (outside the single-domain square) composed of very small (100-nm-sized) ferroelectric domains (see Fig. 1). This situation is to be compared to that of ferromagnetic domains in granular media providing random anisotropy¹⁶. When the lateral scale of the anisotropy is much smaller than the natural magnetic domain size, some averaging takes place and domains do not follow the local anisotropy. The parallel with ferromagnets is possible here as it has been shown that in antiferromagnets, magnetoelastic strains cause imaginary ‘incompatibility elastic charges’ analogous to the surface ‘magnetic’ charges in ferromagnets¹⁷. The corresponding long-range field constitutes the ‘stray’ energy of the sample that governs the appearance of the domain structure. In AF multiferroics, piezoelectric effects in FE domains play exactly this role. Thus, in our as-grown sample, where FE domains are in the 100 nm range, AF domains are larger. In much bigger single FE regions, AF domains have their natural micrometre-size. Perfect locking between the two orders should be expected only when the two characteristic sizes are close. This is evidenced in the following experiment, where we show that the AF order can be modified by locally changing the electrical polarization. Due to magneto-electric coupling, switching the FE variant toggles the direction of magnetic anisotropy, which can induce a rotation of the AF vectors^{18,19}. This is confirmed directly by SHG imaging in a written $8 \times 8 \mu\text{m}^2$ ferroelectric single domain, as shown in Fig. 3. This FE square was first imaged (Fig. 3a) and subsequently electrically manipulated using the PFM tip in two $2.5 \times 2.5 \mu\text{m}^2$ regions (Fig. 3b,c). In the upper one, the in-plane

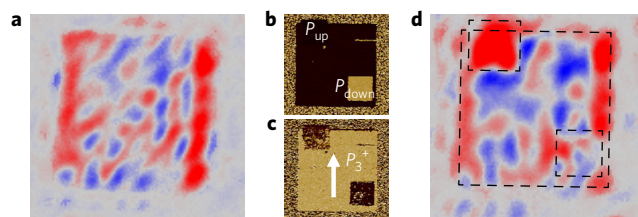


Figure 3 | Imaging magneto-electric coupling. **a**, Reconstructed AF configuration from SHG images of the original ferroelectric single domain. **b,c**, Out-of-plane and in-plane PFM phase images, respectively, of an $8 \times 8 \mu\text{m}^2$ ferroelectric pattern after re-writing two smaller 2.5 by $2.5 \mu\text{m}^2$ squares. The upper left square results from in-plane switching while the lower right square is obtained by out-of-plane switching. **d**, Reconstructed AF configuration from SHG images of the final pattern after FE switching the upper left and lower right corners.

polarization was globally rotated by 90° , while in the lower one, solely the out-of-plane component is reversed. It is clear that the AF domains have accordingly changed (Fig. 3d), thus demonstrating that the AF topography is directly affected by the direction of \mathbf{P}_s . Interestingly, the upper square corresponds to an AF single domain, confirming that when the FE is on a length scale similar to that typical of the AF order, a one-to-one correlation can be achieved.

To go beyond the effect of the FE polarization on the AF order of multiferroics, we have carried out another set of experiments on a region composed of a $10 \times 10 \mu\text{m}^2$ FE single domain with additional inner structures, as shown in Fig. 4. The effect of temperature is first assessed by heating the BFO layer to about 570 K—that is, close to its Néel temperature²⁰. Comparing the AF configuration before (Fig. 4c) and after (Fig. 4d), it is clear that even if some similarities remain, the AF pattern has mostly been re-initialized. More interestingly, one could expect that even sub-coercive electric fields should affect the AF texture through a term in $\mathbf{E} \cdot \mathbf{L}^2$ in the free energy²¹. Other terms in $\mathbf{E}_i \mathbf{L}_j \mathbf{M}_k$ (with i, j, k the space directions) couple to the uncompensated moment \mathbf{M} of strained BFO (ref. 22), and since \mathbf{M} is small these contributions are likely to be negligible. To test this idea, with the PFM tip we applied a linearly increasing electric field during a subsequent scan of the FE pattern. The out-of-plane field was kept in the same direction as the existing P_{up} polarization, but the in-plane trailing field ramped from 1 V to 12 V from the top to the bottom of the square. Comparing Fig. 4d and e, it can be seen that the AF configuration has globally changed from about 2 V onwards (trailing field estimated below 5 MV m^{-1}), while the polarization domains only start to be modified near 11 V (not shown). The line scans in Fig. 4g,h confirm that 3 V is the threshold for changing the AF configuration. Interestingly, the inner square, where the sub-coercive trailing field (vertical) was perpendicular to the in-plane projection of \mathbf{P} , is the one that changed most. It is to be noted that this component is the only one lifting the degeneracy between red and blue domains. Despite the possible weakness of magneto-electric interactions, domain walls can therefore be displaced as their pinning energy seems to be easily overcome. This may not be the case for nucleation of a minority domain. Moreover, the specific nature of the domain walls, where magnetization and polarization can be very different from those of the domains themselves²³, could also influence how domains get modified by sub-coercive fields.

Lastly, it is interesting to note that an intense light can also apply an electric field, by virtue of the optical rectification process²⁴. This stems from the second-order nonlinearity also giving rise to the SHG signal. Short laser pulses of 100 fs duration were used to generate a terahertz electrical pulse in the sample. As this matches the range of the AF resonance in BiFeO_3 , one could expect a much enhanced efficiency compared to that of a d.c. electric field. This is indeed what is observed in Fig. 4f, where again the AF pattern

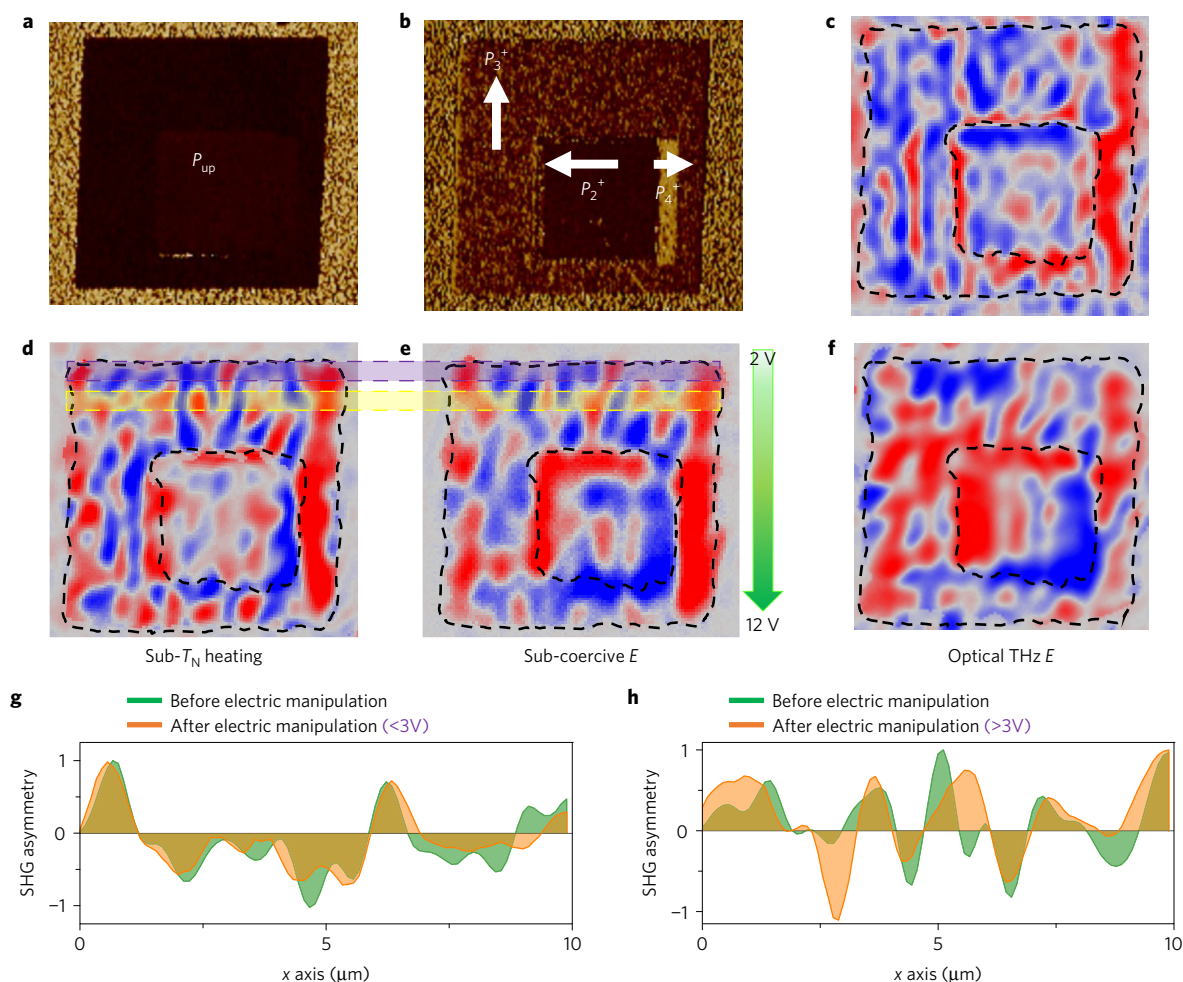


Figure 4 | Manipulation of the AF order in BiFeO₃. **a, b**, Out-of-plane and in-plane PFM phase images, respectively, of a $10 \times 10 \mu\text{m}^2$ square ferroelectric single domain with inner structures providing three polarization variants: P_3^+ , P_2^+ and P_4^+ . **c–f**, Reconstructed AF configurations of the patterns are shown in: virgin state (**c**); after heating to 570 K (**d**); after applying a sub-coercive in-plane electric trailing field swept from 2 V (top) to 12 V (bottom) (**e**) and after sub-coercive picosecond electric pulses delivered by rectification of intense laser pulses (**f**). **g, h**, Line scans at 2 V and 4 V, respectively, during the experiment with the d.c. trailing field (**d** and **e**), confirming the changes in AF domains above 3 V.

has significantly changed after tripling the intensity of our incident beam (electric pulse estimated near 0.1 MV m^{-1}). Note that, at the wavelength used here (925 nm), photon absorption is small and the resulting heating negligible (we measure a 9 K temperature increase on the timescale of minutes). Thus, one can envisage controlling the AF order in a contactless manner using ultrafast light pulses for an all-optical information technology approach.

In summary, we report here a comprehensive study of the AF textures in BiFeO₃ epitaxial layers by SHG imaging and their evolution when subjected to different stimuli. Remarkably, we demonstrate that the micrometre-sized AF domains can be modified by applying sub-coercive electrical fields with an enhanced efficiency when in the terahertz range. Beyond the new insight this provides on the intimate nature of magneto-electric coupling at the microscopic scale, it opens the door for independently controlling ferroelectric and antiferromagnetic writing. This permits one to envisage a two-level coding where classical FE information can be complemented by a built-in very discrete AF message, as well as ultrafast, all-optical writing.

Methods

Methods, including statements of data availability and any associated accession codes and references, are available in the [online version of this paper](#).

Received 21 September 2016; accepted 27 March 2017;
published online 8 May 2017

References

- Jungwirth, T., Marti, X., Wadley, P. & Wunderlich, J. Antiferromagnetic spintronics. *Nat. Nanotech.* **11**, 231–241 (2016).
- Fiebig, M., Pavlov, V. V. & Pisarev, R. V. Second-harmonic generation as a tool for studying electronic and magnetic structures of crystals: review. *J. Opt. Soc. Am. B* **22**, 96–118 (2005).
- Yamada, T., Saito, S. & Shimomura, Y. Magnetic anisotropy, magnetostriction, and magnetic domain walls in NiO. II. Experiment. *J. Phys. Soc. Japan* **21**, 672–680 (1966).
- Catalan, G. & Scott, J. F. Physics and applications of bismuth ferrite. *Adv. Mater.* **21**, 2463–2485 (2009).
- Park, B. G. *et al.* A spin-valve-like magnetoresistance of an antiferromagnet-based tunnel junction. *Nat. Mater.* **10**, 347–351 (2011).
- Wadley, P. *et al.* Electrical switching of an antiferromagnet. *Science* **351**, 587–590 (2016).
- Arai, K. *et al.* Three-dimensional spin orientation in antiferromagnetic domain walls of NiO studied by X-ray magnetic linear dichroism photoemission electron microscopy. *Phys. Rev. B* **85**, 104418 (2012).
- Hillebrecht, F. U. *et al.* Magnetic moments at the surface of antiferromagnetic NiO(100). *Phys. Rev. Lett.* **86**, 3419 (2001).
- Zhao, T. *et al.* Electrical control of antiferromagnetic domains in multiferroic BiFeO₃ films at room temperature. *Nat. Mater.* **5**, 823–829 (2006).
- Fiebig, M., Lottermoser, Th., Frölich, D., Goltsev, A. V. & Pisarev, R. V. Observation of coupled magnetic and electric domains. *Nature* **419**, 818–820 (2002).

11. Fiebig, M. *et al.* Determination of the magnetic symmetry of hexagonal manganites by second harmonic generation. *Phys. Rev. Lett.* **84**, 5620 (2000).
12. Sando, D. *et al.* Crafting the magnonic and spintronic response of BiFeO₃ films by epitaxial strain. *Nat. Mater.* **12**, 641–646 (2013).
13. Ederer, C. & Spaldin, N. A. Weak ferromagnetism and magnetoelectric coupling in bismuth ferrites. *Phys. Rev. B* **71**, 060401(R) (2005).
14. Balke, N. *et al.* Deterministic control of ferroelastic switching in multiferroic materials. *Nat. Nanotech.* **4**, 868–875 (2009).
15. Trassin, M., De Luca, G., Manz, S. & Fiebig, M. Probing ferroelectric domain engineering in BiFeO₃ thin films by second harmonic generation. *Adv. Mater.* **27**, 4871–4876 (2015).
16. Hertzner, G. in *Handbook of Magnetism and Advanced Magnetic Materials* Vol. 4 (eds Kronmüller, H. & Parkin, S.) (John Wiley, 2007).
17. Gomonay, H. & Loktev, V. M. Magnetostriction and magnetoelastic domains in antiferromagnets. *J. Phys. Cond. Matter* **14**, 3959 (2002).
18. Lebeugle, D. *et al.* Electric-field-induced spin-flop in BiFeO₃ single crystals at room-temperature. *Phys. Rev. Lett.* **100**, 227602 (2008).
19. Heron, J. T. *et al.* Deterministic switching of ferromagnetism at room temperature using an electric field. *Nature* **516**, 370–373 (2014).
20. Infante, I. C. *et al.* Bridging multiferroic phase transitions by epitaxial strain in BiFeO₃. *Phys. Rev. Lett.* **105**, 057601 (2010).
21. Ramirez, M. O. *et al.* Magnon sidebands and spin-charge coupling in bismuth ferrite probed by nonlinear optical spectroscopy. *Phys. Rev. B* **79**, 224106 (2009).
22. Kadomtseva, A. M. *et al.* Phase transitions in multiferroic BiFeO₃ crystals, thin-layers, and ceramics: enduring potential for a single phase, room-temperature magnetoelectric 'holy grail'. *Phase Trans.* **79**, 1019–1042 (2006).
23. Catalan, G., Seidel, J., Ramesh, R. & Scott, J. F. Domain wall nanoelectronics. *Rev. Mod. Phys.* **84**, 119 (2012).
24. Talbayev, D., Lee, S., Cheong, S.-W. & Taylor, A. J. Terahertz wave generation via optical rectification from multiferroic BiFeO₃. *Appl. Phys. Lett.* **93**, 212906 (2008).

Acknowledgements

The research leading to these results received funding from the 'Région Ile de France' under the contract 'CALPHOSPIN', from the 'Agence Nationale de la Recherche' project MULTIDOLLS (ANR-12-BS04-0010-02) and from the 'programme transversal nanosciences Acospin'. We would also like to thank R. Belkhou, A. Mougin and A. Thiaville for the loan of some equipment and C. Mocuta for crystallographic measurements on the films. We acknowledge fruitful discussions with F. Charra, C. Fiorini, A. Zvezdin and M. Fiebig as well as invaluable technical support from G. LeGoff and G. Cannies. Lastly, we thank B. Dkhil and M. Bibes for a critical reading of the manuscript.

Author contributions

J.-Y.C., E.H. and M.V. performed the SHG measurements and analysis. J.-Y.C. and M.V. developed the SHG setup. S.F. performed the PFM measurements and analysis. C.C. grew and characterized the BFO samples. J.-Y.C., S.F. and M.V. wrote the manuscript. All authors contributed to the discussions.

Additional information

Supplementary information is available in the [online version of the paper](#). Reprints and permissions information is available online at www.nature.com/reprints. Publisher's note: Springer Nature remains neutral with regard to jurisdictional claims in published maps and institutional affiliations. Correspondence and requests for materials should be addressed to M.V.

Competing financial interests

The authors declare no competing financial interests.

Methods

The SHG experimental setup is based on 100 fs laser pulses emitted from an amplified Ti-Sapphire laser whose wavelength can be continuously adjusted by optical parametric amplification from 2,600 nm to 530 nm (0.47 eV–2.34 eV). The linear polarization of emitted laser pulses is optimized using a Glan polarizer, and its polarization direction can be continuously rotated using a $\lambda/2$ prism. The SHG light emitted from the sample is then imaged onto a Peltier-cooled charge-coupled device (CCD) camera (-15°C) using an objective lens ($\times 50$ N.A. = 0.7). The obtained optimum SHG spatial resolution is between 350 nm and 500 nm for an incident beam wavelength ranging from 800 nm to 1,100 nm.

To analyse the SHG experimental data, the tensors have to be expressed in the laboratory frame (x, y, z). For example, considering the orientation of the ferroelectric variant in the single domain (region 1), tensors should be rotated around the X_2 -axis of the crystal frame which is at an angle $\alpha = \cos^{-1}(1/\sqrt{3})$ to the y -axis of the laboratory frame.

The point-group symmetry of the crystal structure alone is 3m so that the second-order time-invariant susceptibility tensor has the following symmetry in the crystal frame (X_1, X_2, X_3), with X_3 the ferroelectric axis and X_2 taken in the direction of a mirror plane:

$$\chi^{(i)} = \begin{bmatrix} \chi_{111}^{(i)} & -\chi_{111}^{(i)} & 0 & 0 & \chi_{113}^{(i)} & 0 \\ 0 & 0 & 0 & \chi_{113}^{(i)} & 0 & -\chi_{111}^{(i)} \\ \chi_{113}^{(i)} & \chi_{113}^{(i)} & \chi_{333}^{(i)} & 0 & 0 & 0 \end{bmatrix}$$

Below the Néel temperature (about 640 K in the bulk), the appearance of AF order leads to a breaking of time-reversal symmetry. In a single AF domain, magnetic moments are expected to be along a specific direction in the plane perpendicular to the ferroelectric polarization, which lifts the three-fold rotation symmetry around X_3 and lowers the symmetry to monoclinic, with magnetic point-group m. Three AF variants should exist (reflecting the original rhombohedral crystallographic symmetry) which define the orientation of the mirror plane (orthogonal to the AF vector direction, parallel to \mathbf{P}_S). Taking this direction as X_2 , the second-order time-noninvariant susceptibility tensor reads:

$$\chi^{(c)} = \begin{bmatrix} \chi_{111}^{(c)} & \chi_{122}^{(c)} & \chi_{133}^{(c)} & 0 & \chi_{113}^{(c)} & 0 \\ 0 & 0 & 0 & \chi_{223}^{(c)} & 0 & \chi_{122}^{(c)} \\ \chi_{113}^{(c)} & \chi_{223}^{(c)} & \chi_{333}^{(c)} & 0 & \chi_{133}^{(c)} & 0 \end{bmatrix}$$

The two other possible orientations of the AF vector are obtained by rotating the susceptibility tensor by $\pm 120^\circ$ around X_3 .

To understand the experiment, the induced SHG dipole is to be expressed in the laboratory (x, y, z)-frame. After some calculation, one finds for the x component of the time-invariant part of the induced SHG electric dipole:

$$P_x^{(i)} = A \cos^2 \varphi + B$$

where A and B are linear functions of χ_{111} , χ_{113} and χ_{333} . As for the time-noninvariant part of the induced SHG dipole, three dependences can be identified depending on the AF domains:

$$P_{x_type1}^{(c)} = a_1 \cos^2 \varphi + b_1 \cos \varphi \sin \varphi + c_1$$

$$P_{x_type2}^{(c)} = a_1 \cos^2 \varphi - b_1 \cos \varphi \sin \varphi + c_1$$

$$P_{x_type3}^{(c)} = a_3 \cos^2 \varphi + c_3$$

where a_1 , b_1 , c_1 , a_3 and c_3 are linear functions of the time-noninvariant tensor components.

Sample preparation. The epitaxial thin film heterostructure was grown by pulsed laser deposition using a KrF excimer laser with $\lambda = 248$ nm, $\sim 1 \text{ J cm}^{-2}$ on a SrTiO₃ (001) single-crystal substrate. The 25-nm-thick SrRuO₃ bottom electrode was grown with a 5 Hz repetition rate at 650 °C under 150 mtorr of oxygen. The 110-nm-thick BiFeO₃ film was subsequently grown at 650 °C under 270 mtorr of oxygen with a 1 Hz repetition rate. The sample was slowly cooled down under high oxygen pressure.

Characterization. PFM experiments were conducted with an atomic force microscope (Nanoscope V multimode, Bruker) feeding two external SR830 lock-in detectors (Stanford Research) for simultaneous acquisition of in-plane and out-of-plane responses. A DS360 external source (Stanford Research) was used to apply the a.c. excitation to the SrRuO₃ bottom electrode at a frequency of 35 kHz, while the conducting Pt coated tip was grounded. For poling experiments, a d.c. bias was applied to the SrRuO₃. The different in-plane variants of the polarization were selected by aligning the microscope slow-scan axis with the targeted variant.

Data availability. All relevant data are available from the authors, and/or are included with the manuscript.